Temporal changes in rock-uplift rates of folds in the foreland of the Tian Shan and the Pamir from geodetic and geologic data

Aaron Bufe[1,2*], David P.S. Bekaert[3], Ekbal Hussain[4], Bodo Bookhagen[2,5], Douglas W. Burbank[1,2], Jessica A. Thompson Jobe[2,6], Chen Jie[7], Li Tao[7,8], Liu Langtao[7,9], Weijun Gan[7]

[1]Department of Earth Sciences, University of California, Santa Barbara, California, 93106, USA
[2]Earth Research Institute, University of California, Santa Barbara, California, 93106, USA
[3]Jet Propulsion Laboratory, California Institute of Technology, Pasadena, California, USA.
[4]School of Earth and Environment, University of Leeds, Leeds, UK.
[5]Institute of Earth and Environmental Science, University of Potsdam, Potsdam-Golm, Germany.
[6]Institute of Tectonic Studies, Department of Geological Sciences, University of Texas, El Paso, Texas, 79902, USA
[7]State Key Laboratory of Earthquake Dynamics, Institute of Geology, China Earthquake Administration, Beijing China.
[8]School of Earth Science and Engineering, Sun Yat-Sen University, Guangzhou, 510275, China
[9]Department of Earth Science and Engineering, Hebei University of Engineering, Handan, China

*E-mail: bufe@umail.ucsb.edu

1 June 2017

Re-Submitted to GRL

Key Points

- Decomposition of InSAR data reveals spatial variations of uplift rates on folds in the foreland of the Tian Shan and Pamir in NW China
- Piece-wise linear fits to geodetic and geologic uplift rates constrain temporal evolutions of uplift rates on five active folds
- Our observations confirm propagation of deformation from the Tian Shan and Pamir mountain fronts into the Tarim Basin

Accepted Article

This article has been accepted for publication and undergone full peer review but has not been through the copyediting, typesetting, pagination and proofreading process which may lead to differences between this version and the Version of Record. Please cite this article as doi: 10.1002/2017GL073627

© 2017 American Geophysical Union. All rights reserved.

Abstract

Understanding the evolution of continental deformation zones relies on quantifying spatial and temporal changes in deformation rates of tectonic structures. Along the eastern boundary of the Pamir-Tian Shan collision zone, we constrain secular variations of rock-uplift rates for a series of five Quaternary detachment- and fault-related folds from their initiation to the modern day. When combined with GPS data, decomposition of interferometric synthetic aperture radar time-series constrains the spatial pattern of surface- and rock-uplift on the folds deforming at decadal rates of 1-5 mm/y. These data confirm the previously proposed basinward propagation of structures during the Quaternary. By fitting our geodetic rates and previously published geologic uplift rates with piecewise-linear functions, we find that gradual rate changes over >100 ky can explain the InSAR observations where changes in average uplift rates are greater than ~1 mm/y among different time-intervals (~10^1, $10^{4\text{-}5}$, $10^{5\text{-}6}$ y).

1 Introduction

Deformation rates along individual tectonic structures underpin our understanding of the dynamics of continental deformation zones and their seismic hazards. Whereas the mechanics for many types of folds and faults are well understood [*Suppe*, 1983; *Suppe and Medwedeff*, 1990; *Epard and Groshong Jr*, 1995; *Poblet and McClay*, 1996; *Allmendinger*, 1998; *Li et al.*, 2013; *Yan et al.*, 2016], commonly unknown temporal and spatial differences in deformation rates complicate the reconstruction of the kinematic history of deformation zones. After initiation, faults and folds tend to lengthen with annual rates of lateral propagation ranging from a few millimeters to several centimeters [*Burbank et al.*, 1996; *Jackson et al.*, 2002; *Chen et al.*, 2007], until they encounter barriers that pin the tips of the structure [*Dawers et al.*, 1993; *Manighetti et al.*, 2001; *Amos et al.*, 2010]. Commonly, a near block-like pattern of incremental (or instantaneous) slip is assumed with spatially constant slip rate along the structure, rapidly decreasing to zero at the tips [*Manighetti et al.*, 2001; *Amos et al.*, 2010]. Nonetheless, block-like incremental slip is not necessary and spatially varying deformation rates have been shown to occur, for example, along laterally tilting folds [*Li et al.*, 2013], propagating structures [*Amos et al.*, 2010] or segmented ones [*Dawers et al.*, 1993; *Anders and Schlische*, 1994; *Davis et al.*, 2005]. In addition to spatial variations of slip rates, deformation varies temporally. Changes in the distribution of strain across fault zones and mountain ranges [*Thompson et al.*, 2002; *Oskin et al.*, 2007], foreland propagation of

© 2017 American Geophysical Union. All rights reserved.

Accepted Article

deformation [*Hubert-Ferrari et al.*, 2007; *Heermance et al.*, 2008], propagation of asperities along structures [*Hilley and Arrowsmith*, 2008], loading or unloading of the crust by water or ice [*Hampel et al.*, 2007], or reorganization of strain across plate boundaries [*Friedrich et al.*, 2003; *Allen et al.*, 2004; *Sobel et al.*, 2006; *Molnar and Stock*, 2009; *Clark*, 2012] can cause decadal to million-year variations in slip rates. Moreover, stochastic or cyclic temporal variations in deformation rates can occur due, for example, to the clustering of strain release [*Grant and Sieh*, 1994; *Marco et al.*, 1996; *Friedrich et al.*, 2003; *Meade and Hager*, 2004; *Dolan et al.*, 2007; *Oskin et al.*, 2008], seasonal water loading [*Bettinelli et al.*, 2008], or changes throughout a seismic cycle [*Thatcher*, 1984; *Cattin and Avouac*, 2000; *Hilley et al.*, 2009].

Slip-rate variations of single structures on geologic timescales are inferred from rate measurements across multiple time-intervals and, in the absence of additional evidence, are commonly described as step-like changes [*Hubert-Ferrari et al.*, 2007; *Oskin et al.*, 2007; *Heermance et al.*, 2008; *Gold and Cowgill*, 2011; *Gold et al.*, 2017]. Whereas measuring gradual rate-changes requires a data density that is commonly not available [*Gunderson et al.*, 2014], an assumed functional form can typically be fitted to existing measurements [*Gourmelen et al.*, 2011].

From a decomposition of interferometric synthetic aperture radar (InSAR) time-series and GPS data, we constrain patterns of surface-uplift rates for a series of Quaternary contractional structures along the rapidly deforming eastern boundary of the Pamir-Tian Shan collision zone. Assuming uplift of sparsely eroded surfaces to be equivalent to rock uplift, these data are then compared with geologic rates. In addition to fitting temporal changes in uplift rates with step functions, we impose piece-wise linear functions of temporal uplift-rate changes and explore a range of possible alternative velocity variations with a Monte Carlo model .

2 Geologic setting

The Pamir and Tian Shan jointly accommodate 20-25 mm/y: nearly 50% of the total Indo-Asian shortening rate [*Abdrakhmatov et al.*, 1996; *Zubovich et al.*, 2010] (Fig. 1). About 11±3 mm/y of present-day shortening is taken up across the ~70±10-km-wide boundary between the two orogens (Figs. 1a, b). At the eastern edge of the Pamir, deformation along the Main Pamir Thrust appears to have mostly ceased [*Chen et al.*, 2011; *Sobel et al.*, 2011; *Thompson et al.*, 2015] and stepped northward, where it interferes with the southern Tian

© 2017 American Geophysical Union. All rights reserved.

Accepted Article

Shan (Fig. 1c). Here, the Pamir Frontal Thrust (PFT), the Mingyaole fold, and the Mushi fold accommodate a total Late Quaternary shortening of ~6-7 mm/y [*Li et al.*, 2012; 2013; 2015]. To the east of the PFT, deformation along the Tarim basin-Tian Shan boundary has stepped southward from the South Tian Shan thrust into the Kashi foreland basin over the past 25 My, causing the initiation, growth, and abandonment of a series of southward-younging structures (Fig. 1c) [*Heermance et al.*, 2008]. Modern deformation occurs on a series of anticlines: the Kashi, Atushi, and Mutule folds (Fig. 1c) that have each accommodated >2-3 mm/y of shortening since their initiation 1-2 My ago [*Scharer et al.*, 2004; *Chen et al.*, 2007]. Structures to the north of these folds, such as the Keketamu and Tashipisake anticlines, lack deformed Late Quaternary surfaces and appear to be mostly inactive [*Heermance et al.*, 2008].

3 Methods and data

InSAR time-series analysis of Envisat-ASAR data from two ascending tracks (55 and 284) and two descending tracks (191 and 420) was performed using the Stanford Method for Persistent Scatterers (StaMPS) [*Hooper et al.*, 2004; 2012] (Fig. S1, Table S1). Interferograms from the Envisat scenes acquired between 2003-2010 were generated using the ROI_PAC [*Rosen et al.*, 2004] and DORIS [*Kampes and Usai*, 1999] packages, topography was removed with a 90-m-resolution SRTM digital elevation model [*Farr et al.*, 2007], and atmospheric phase delays were corrected with the Toolbox for Reducing Atmospheric InSAR Noise (TRAIN) [*Dee et al.*, 2011; *Bekaert et al.*, 2015a; 2015b] (Figs. S2-4). An interpolated northward velocity field from published GPS data [*Zubovich et al.*, 2010], together with ascending and descending InSAR time-series, was then used to reference the InSAR velocities to stable Eurasia and to decompose the geodetic data into eastward and vertical components (Figs. S3-4) [*Hussain et al.*, 2016a; 2016b] (see Text S1 for additional detail). In the remainder of the analysis, we use only the decomposed vertical velocity field as a measure of absolute decadal surface-uplift rates. Peak decadal surface-uplift rates were measured on 10-km-wide swath profiles plotted approximately perpendicular to the strike of thrust faults and/or the trend of fold axes (Figs. S5-7, Table S2). The weighted arithmetic means and corresponding standard errors were calculated in 1-km bins along the length of the 10-km-wide swath profiles. Decadal peak-uplift rates were then specified as the maximum of the binned InSAR velocities across each structure. Where the InSAR data are coherent, significant erosion or sedimentation is unlikely. Therefore, the resulting decadal surface-

© 2017 American Geophysical Union. All rights reserved.

Accepted Article

uplift rates of major tectonic structures are assumed to largely reflect absolute rates of rock uplift with respect to stable Eurasia.

We compiled published initiation ages (0.4-1.6 My) and measured total structural relief (0.6-5.0 km) on published structural cross sections for the Mingyaole [*Chen et al.*, 2005; *Li et al.*, 2015], Kashi [*Chen et al.*, 2007], Atushi [*Scharer et al.*, 2004; *Heermance et al.*, 2008], Mushi [*Li et al.*, 2013; *Thompson*, 2013], and Mutule [*Bufe et al.*, in revision] folds (Table S3, Fig. S8). As an exception, initiation of the Mutule fold, was estimated from the published initiation age of the Atushi fold to the west [*Chen et al.*, 2002; *Scharer et al.*, 2004; *Heermance et al.*, 2008] on the basis of interference between the two structures (Table S3). To account for uncertainties in the position of the outermost hinges and strata thickness, we assign a 2σ uncertainty of ±500 m to all measurements of total structural relief estimated from geologic cross-sections (Table S3, Fig. S8). For each structure, total rock uplift was then divided by the initiation age to obtain an average uplift rate since initiation of growth (Table S3). Finally, we compiled published ages (8.5-80 ky) and heights above the modern river (15-130 m) for uplifted Late Quaternary fluvial deposits that are largely unaffected by erosion and can be assumed equivalent to record both rock and surface uplift [*Heermance et al.*, 2008; *Li et al.*, 2012; *Li et al.*, 2013; *Thompson*, 2013; *Li et al.*, 2015; *Bufe et al.*, in revision] (Table S3). For terraces with ages obtained through both fine-grained quartz optically stimulated luminescence [*Li et al.*, 2012] and cosmogenic radionuclide (CRN) dating [*Thompson*, 2013], we used the CRN dates, because they have been shown to be more reliable in this region [*Thompson*, 2013].

A comparison of uplift rates among multiple structures assumes a common base level. Geologic uplift rates of thrust faults and folds are calculated, where possible, with respect to the surrounding basins (e.g. Fig. S8). Modern rivers serve as a references for river-terrace heights used to estimate uplift rates of folds at kiloyear timescales. These references are assumed to be equivalent to the reference of the modern river. In turn, InSAR vertical velocities have to be recalculated with respect to the basins in the study area. To this end, we estimate the vertical motions of these basins with respect to stable Eurasia using swath profiles drawn perpendicular to the strike of major structures (Figs. S6-7). The estimated background uplift rate of 1.5±0.5 mm/y is fairly consistent across the study area and is subtracted from the InSAR rates when they are compared to geologic uplift rates (Table S2).

Accepted Article

© 2017 American Geophysical Union. All rights reserved.

4 Results

The decomposition of the InSAR time series clearly resolves 10- to 20-km-wide zones of surface uplift centered along nearly all structures in the study area that are interpreted or known to have been active during the Quaternary (Fig. 2). These vertical velocities on active structures are smooth across track boundaries (Fig. 2) and consistent with a recent independently-published decomposition of InSAR in the region [*Qiao et al.*, 2017]. Systematic correlation between InSAR velocities and topography can arise from atmospheric phase delays. The lack of correlation of vertical InSAR velocities with many major topographic features (Figs. 3, S6-7), however, supports the interpretation of a tectonic origin for those structures that do show elevated surface-uplift rates. The large, elliptical uplift signal along the eastern part of the Keketamu anticline north of Atushi (Fig. 2) is present in only one track (Figs. S3-4) and could arise from atmospheric phase delays. Alternatively, the signal could be linked to water injection into the Akmomu gas field (Fig. 2). Significant subsidence centered on the cities of Kashi and Shule (Fig. 2) is probably due to groundwater withdrawal.

We find surface-uplift rates are highest along the Pamir Frontal Thrust (PFT), the Mushi anticline, and the Kashi anticline (Fig. 2). Our data might indicate ongoing uplift along the South Tian Shan Thrust, but the Main Pamir Thrust, as well as the Tian Shan foreland north and east of the Atushi fold (including the Mutule fold), appear to be inactive (Fig. 2). Modest earthquakes ($M \leq 5$) that occurred between 2003-2010 and depths of 9-10 km (Fig. 2) are neither known, nor expected to have produced surface displacements larger than the sensitivity of the InSAR (>4-10 cm over 7 years) [*Bonilla*, 1982; *Biasi and Weldon*, 2006]. Whereas slip-rate variations during a seismic cycle could introduce uncertainties [*Thatcher*, 1984; *Cattin and Avouac*, 2000; *Hilley et al.*, 2009], the observed uplift pattern is consistent with constraints on longer-term geologic uplift rates (Fig. 3), as well as inferred basinward propagation of the deformation front over the past 25 My [*Heermance et al.*, 2008; *Chen et al.*, 2011; *Thompson et al.*, 2015].

Six-km-wide swaths aligned along the axis of each active structure reveal significant spatial variations in decadal surface-uplift rates (Fig. 3). The Kashi and Atushi folds show a broad, bow-shaped pattern with peak rates close to their centers (Fig. 3). Surface-uplift rates decrease at the tips of the folds with a tip-zone spanning 10-25% of the length of the structure. Similar to these two structures, the Mushi fold also shows peak surface-uplift rates close to its center, but the peak is narrower and higher. Whereas post-seismic effects from the

Accepted Article

© 2017 American Geophysical Union. All rights reserved.

nearby 1985 M7.4 Wuqia earthquake to the west of Mushi (Fig. 2) cannot be ruled out, the gradual decrease of surface-uplift rates toward the eastern tip of the fold is consistent with observed lateral tilting of fluvial terraces since at least 130 ka [*Li et al.*, 2013]. In contrast to these well-defined patterns, spatial surface variations of uplift rate along the PFT and the Mingyaole fold are more complex. Uncertainties in the InSAR data, interference of structures, and fault segmentation could cause these variations. Thus, possibly, the tips of the Mingyaole fold uplift faster due to interference with the Kashi fold (to the east) and the PFT (to the west).

Assuming that peak decadal surface-uplift rates on major structures are dominated by rock-uplift, as described above, we find that average rock-uplift rates measured (1) since fold-initiation, (2) across the last 10-80 ky, and (3) across a 7-year (InSAR) interval have either stayed constant or have increased along frontal structures: the PFT and the Mushi and Kashi folds (Figs. 4, S9). In contrast, rock-uplift rates on the more hinterland Mutule and Atushi folds have decreased (Figs. 4, S9). Such spatial patterns are consistent with basinward propagation of peak strain rates [*Heermance et al.*, 2008; *Thompson et al.*, 2015].

5 Monte Carlo modeling of gradually changing rock-uplift rates

Changes in average rock-uplift rate measured across different time intervals, that are each long enough to average across several earthquakes, are commonly obtained by linearly connecting single measurements of cumulative rock-uplift [e.g. *Gold and Cowgill*, 2011] (Fig. S10a). Such fits result in step-like changes in instantaneous uplift rates (Fig. S10b). Sometimes, abrupt velocity changes can be linked to climatic or geologic triggers [*Hampel et al.*, 2007; *Gold et al.*, 2017]. Even if such changes occurred, however, their precise timing is difficult to capture where few sample ages exist. Moreover, gradual changes in deformation velocity of single structures can occur [*Gourmelen et al.*, 2011], for example, from the lateral propagation of a structure with instantaneous rock-uplift rates that drop smoothly to zero toward the tip (Figs. 3a, c-d, S10c-d). Even structures lacking propagating tips might accelerate after initiation and decelerate toward the cessation of deformation [*Gourmelen et al.*, 2011] or vary in a complex sequence of accelerations and decelerations [*Chevalier et al.*, 2005; *Gunderson et al.*, 2014]. Such gradual changes can only be detected in high-resolution uplift-rate datasets obtained, for example, from well-dated terraces [*Bourgois et al.*, 2007]. An unlimitied number of functions can be fit to discrete rock-uplift data calculated across different time-intervals (Fig. S10a). Therefore, in addition to fitting step functions to our data,

© 2017 American Geophysical Union. All rights reserved.

Accepted Article

we explore the range of plausible gradual uplift-rate evolutions for five selected structures by imposing a geologically reasonable piecewise-linear function with an initial phase of velocities increasing from zero ($v_3 = 0$) at the time of initiation (t_3) to an intermediate value (v_2) at some unknown time (t_2) (Fig. 4a), followed by a time of steady velocities ($v_1 = v_2$), and either an increase or decrease at time (t_1) to the final velocity (v_0) at the modern day ($t_0 = 0$) (Fig. 4a). Using a Monte Carlo approach, we randomly pick a parameter set for each of at least 10^5 iterations (Fig. 4, Table S4) and evaluate the goodness of fit of the resulting uplift-rate scenario to the geologic data (See text S2 for additional details). We note, that t_1 and t_2 are each allowed to be zero, equal to t_3, or equal to each other, which includes a range of scenarios such as step functions (Fig. 4b). However, only one time-period is allowed across which velocities are constant, and functions with more complex step-changes cannot be fit with our approach. This limit may bias the model toward fitting gradual rate changes in situations for which the three, mean uplift rates define inconsistent rate changes through time, e.g., a velocity increase followed by a decrease (Fig. 4f) or vice versa (Fig. 4g).

For all folds, curves within 95% of the maximum probability show a variety of likely uplift-rate scenarios (Fig. 4, S11). For structures for which average rock-uplift rates calculated across different time-intervals are similar in magnitude (within <~1 mm/y), near step-like functions of instantaneous uplift rates yield the best fits, but initial acceleration periods of a few 10s-100s of kiloyears are not unlikely (Central Kashi: Fig. 4e, Fig. S12a). In contrast, where average uplift rates measured across Late Quaternary timescales have increased compared to the rate since initiation of the structure, a more gradual change in uplift rate through time is predicted by a higher fraction of model solutions (Mushi, Mingyaole, Eastern Kashi: Figs. 4c-d, 4f, S12b). Finally, where uplift rates have decreased significantly over time, a rapid increase in velocities, followed by a gradual decrease are among the best solutions of the model (Atushi-Mutule: Figs. 4g-i, S12c).

6 Discussion

In this study, decomposition of InSAR data resolves surface-uplift rates of individual, ≤10-km-wide structures over the past decade along the Tian Shan-Pamir interface in unprecedented detail. The correlation of decadal surface-uplift rates with geologic outlines of the structures, the absence of a strong correlation between elevation and InSAR velocities, the consistency of peak surface-uplift rates across track boundaries, and their smooth variation along the structure support the interpretation of a tectonic origin for the InSAR

© 2017 American Geophysical Union. All rights reserved.

Accepted Article

signal on the PFT, and the Mushi, Mingyaole, Kashi, Atushi, and Mutule folds (Fig. 2). The consistency between the broad spatial patterns of geologic and geodetic uplift rates on the structures (Fig. 3) suggests that large-scale (>10s of kms) patterns of decadal velocities can inform longer-term trends, although it remains problematic to assess the effects of short term velocity variations due, for example, to changes across an earthquake cycle, with such a simple rate comparison. Our data confirm previous findings of the basinward propagation of tectonic activity and lend further support to the assumed, but debated, inactivity of the Main Pamir Thrust [*Sobel et al.*, 2011; *Li et al.*, 2012; *Thompson et al.*, 2015] and of the northern Tian Shan foreland [*Heermance et al.*, 2008].

The background surface uplift rate of 1.5±0.5 mm/y (Figs. 2, S6-7) arises from tying the InSAR data to the stable Eurasian reference frame using GPS data (Text S1). Because the rate is within uncertainties of the GPS vertical velocities (>2 mm/y), its significance remains unknown. Here, for all analyses, the background rate is subtracted from the InSAR measurements and does not affect the comparison between InSAR and geologic rates.

The arc-shaped spatial pattern of decadal surface- and rock-uplift rates along the Kashi, Atushi, and Mushi folds with "tip zones" in which vertical velocities are smoothly dropping to zero (Fig. 3) is inconsistent with a pure block-shape model of incremental surface uplift [*Manighetti et al.*, 2001]. Instead, it favors interpretations in which uplift rates change more gradually along strike (Fig. S10). Where such gradual, along strike changes occur, lateral propagation of "tip zones" can lead to temporal changes of instantaneous uplift rates for any point through which the tip propagates (Fig. S10c-d). Lateral propagation rates of ~40 and ~50 mm/y have been inferred for the tips of the Kashi and Atushi folds, respectively [*Scharer et al.*, 2004; *Chen et al.*, 2007]. Thus, with a tip zone length of 10±5 km and assuming that this spatial pattern was constant through time, a point on the Kashi or Atushi fold would be expected to accelerate for at least 200±100 ky or 250±130 ky, respectively. Such time scales of acceleration are consistent with the modeled uplift-rate scenarios (Fig. 4), although some of the most probable fits to the Atushi data predict shorter periods of acceleration (Figs. 4f-g).

Where structures interfere (Mingyaole fold), are segmented (PFT), or tilt laterally (Mushi fold), the spatial pattern of decadal uplift rates is more complicated (Fig. 3) and such complexity makes the interpretation of a "representative" modern velocity challenging. Moreover, with only three data points for uplift rates across a time interval of 0.5-1.6 My on any given fold, considerable uncertainties remain on a fold's temporal uplift-rate evolution. Nevertheless, our modeling framework yields ranges of probable temporal variations in

Accepted Article

© 2017 American Geophysical Union. All rights reserved.

uplift-rates that are distinct for different structures and can constrain a range of likely kinematic evolution of contractional structures.

7 Conclusions

With a decomposition of InSAR data, we obtain insights into the spatial patterns of decadal surface- and rock-uplift rates along rapidly deforming contractional structures at the Tian Shan-Pamir interface and observe spatial patterns of fold uplift that are inconsistent with block-like deformation patterns. We compile published geologic uplift rates and use step-wise and piecewise-linear fitting of geodetic and geologic uplift rates to reveal temporal patterns of deformation in the study area. Our observations confirm the propagation of deformation away from the mountain fronts and into the Tarim Basin over the past 2 My.

8 Acknowledgements

We acknowledge ESA for providing the ASAR images and technical support. This work benefited from discussions with Tim Wright, Daniel Wissmann, Miriam Dünforth, Cengiz Yildirim, Steffanie Rieger, and Markus Hoffmann. Careful reviews of the work by Romain Jolivet, Ryan Gold, and an anonymous reviewer improved an early version. A DAAD graduate student award and a UCSB Regents Special Fellowship to A.B., as well as National Science Foundation grant 1050070 to D.W.B. and B.B., and the LED2016A05 grant to C.J., L.T. and L.L. are gratefully acknowledged. D.P.S.B. was sponsored by the Jet Propulsion Laboratory, California Institute of Technology, under a contract with the National Aeronautics and Space Administration. Shapefiles of interferometric data as well as codes for the Monte Carlo modeling can be found in the supporting information. Additional detail and primary sources for the geologic data used in the analysis are included in Figure S8 and Table S3.

Accepted Article

© 2017 American Geophysical Union. All rights reserved.

Accepted Article

9 Figures

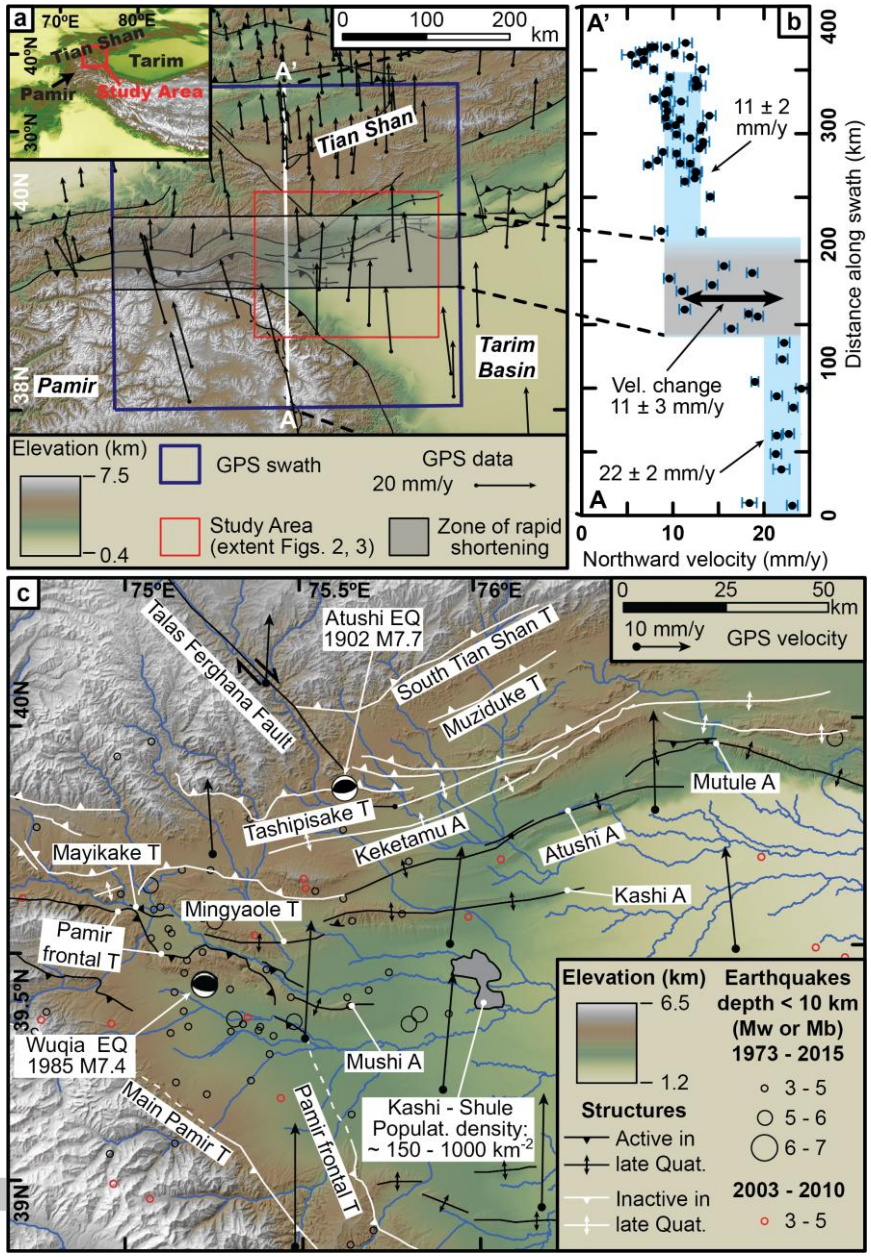

Figure 1: Overview of the study area. (a) Regional map of the Pamir and Tian Shan with horizontal GPS velocities [*Zubovich et al.*, 2010]. (b) Northward component of the GPS velocity in the 400 km-wide swath along A-A'. (c) Digital elevation model of the study area showing a series of faults and folds in the foreland of the Tian Shan and Pamir. Late Quaternary activity of structures (black and white lines) is based on geologic evidence published in previous studies [*Chen et al.*, 2007; *Heermance et al.*, 2008; *Li et al.*, 2012; *Li et al.*, 2013; *Li et al.*, 2015; *Thompson et al.*, 2015]. Earthquake locations are from the USGS earthquake catalog except for the Wuqia event [*Feng*, 1994] and the Kashi event [*Kulikova*, 2015]. A: Anticline; T: Thrust.

© 2017 American Geophysical Union. All rights reserved.

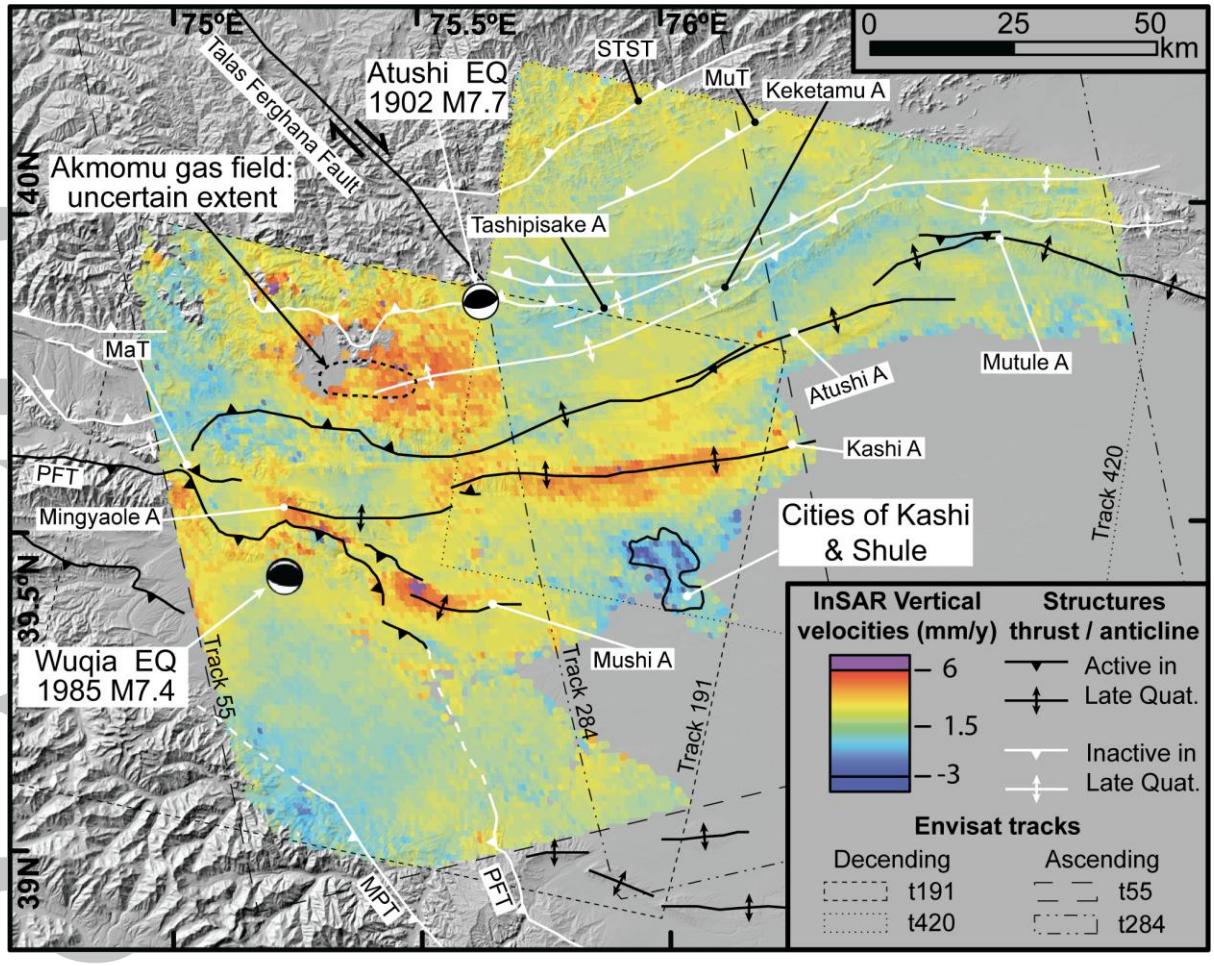

Figure 2: Decadal uplift rates from InSAR time-series analysis of Envisat data for two ascending, and two descending tracks. PFT: Pamir Frontal Thrust; MPT: Main Pamir Thrust; MaT: Mayikake Thurst; MuT: Muziduke Thrust; STST: South Tian Shan Thrust. A: Anticline.

Accepted Article

© 2017 American Geophysical Union. All rights reserved.

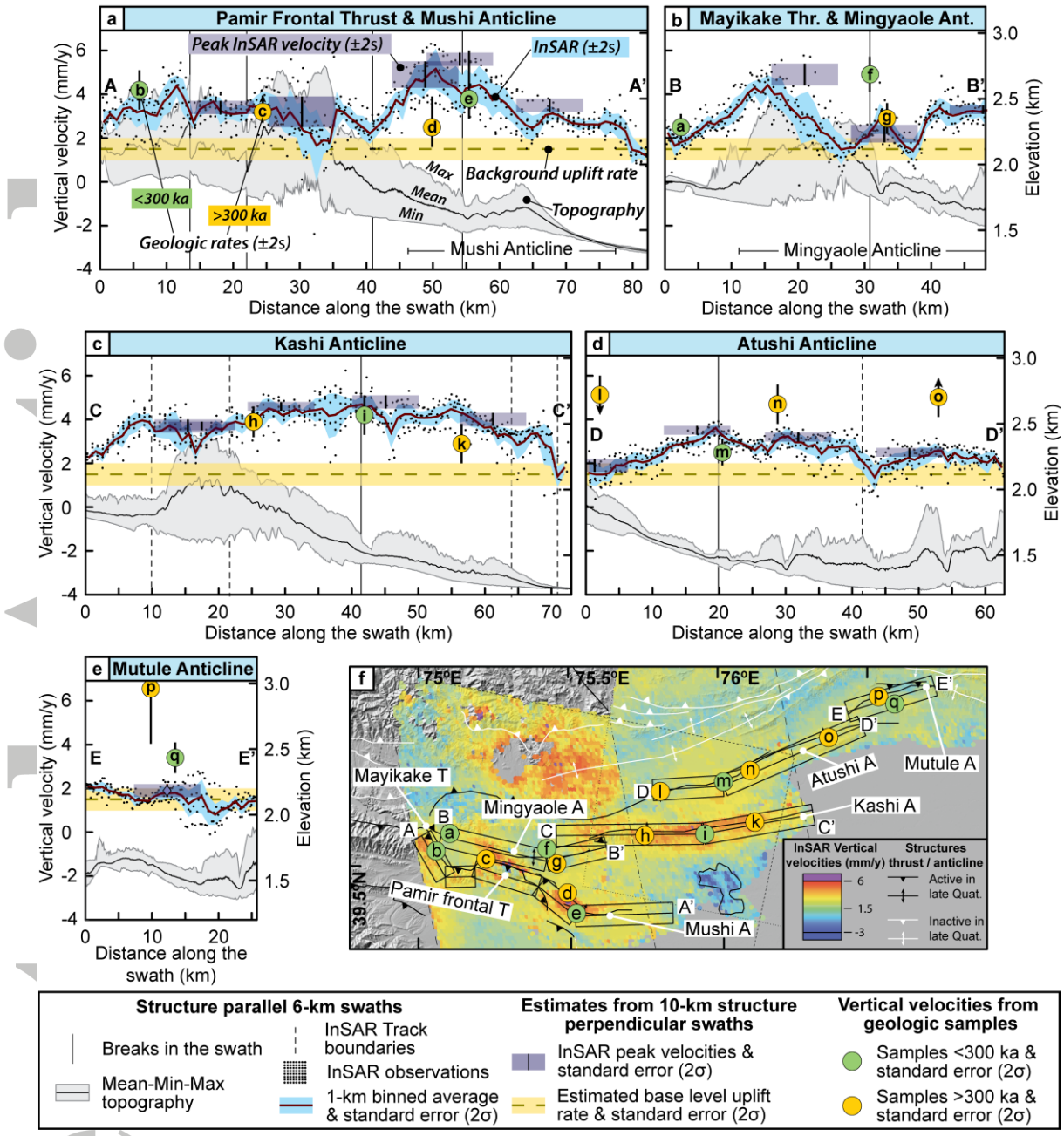

Figure 3: Along-strike changes in rock-uplift rates. (a-e) Six-km-wide swath profiles along strike of the study area's major active structures show decadal vertical velocities and associated topography. Mean and standard error of the InSAR velocities are calculated in 1-km bins (approximate spacing of points in the InSAR velocity map). Yellow horizontal bars mark background uplift rate of 1.5±0.5 (±2σ) mm/y (see text and Figs. S6-7). Peak geodetic uplift rates (±2σ) were measured on these same swaths (Figs. S6-7). Yellow and green points are geologic uplift rates compiled from the published literature (Table S3). For illustration purposes, the background uplift rate in the InSAR velocity field was added to the geologic rates (Table S3). (f) Overview map with profile locations and locations where geologic uplift rates were calculated. A: Anticline; T: Thrust.

© 2017 American Geophysical Union. All rights reserved.

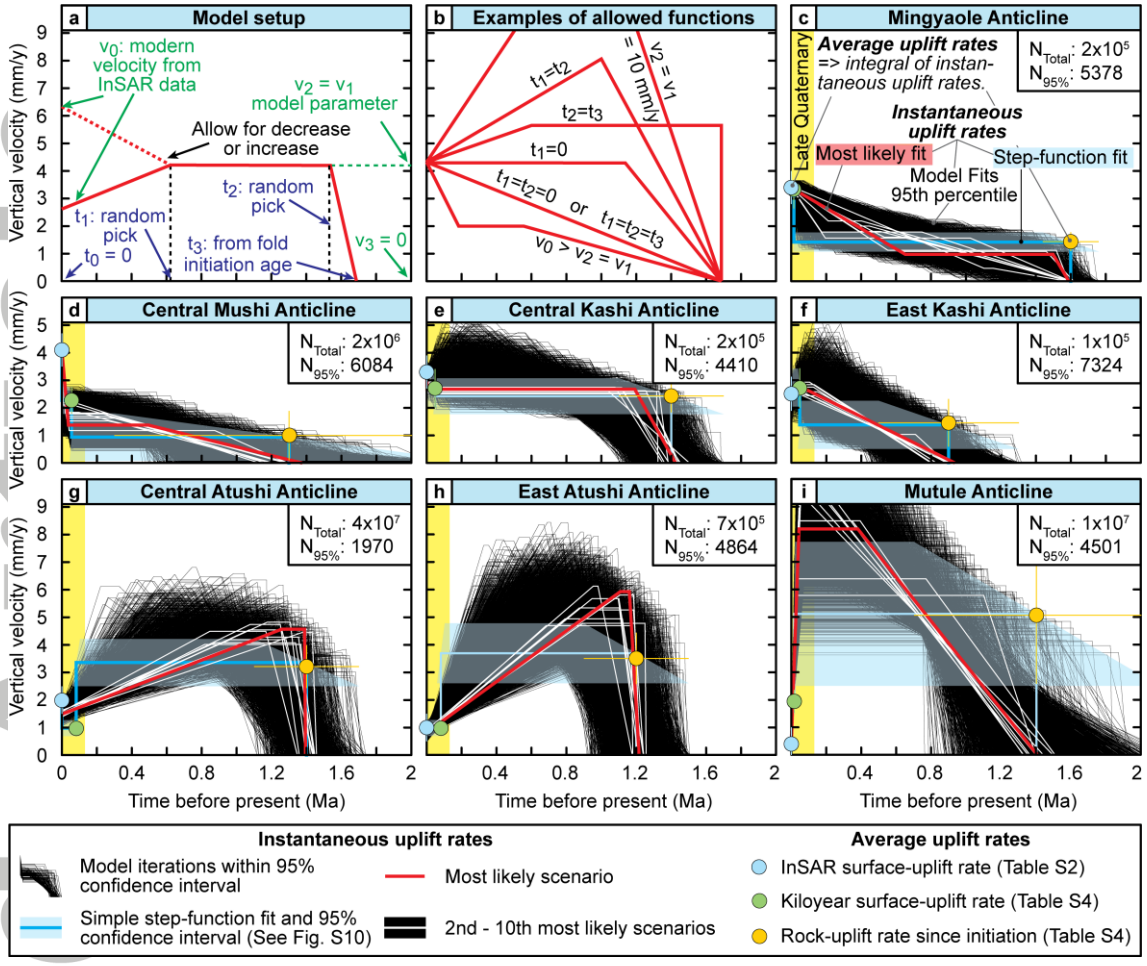

Figure 4: Results from uplift-rate modeling on Mingyaole, Mushi, Kashi, Atushi, and Mutule. (a) Conceptual sketch showing all model parameters. (b) Examples of functional forms allowed by the model. (c-i) Results from modeling showing all scenarios with probabilities within 5% of the maximum probability (black lines). The single most likely scenario is shown in red. The next nine most likely scenarios are shown in white. A step-function fitS10 is shown in blue. Green and yellow data points are average geologic rock-uplift rates from the published literature (Table S3), blue data points are average geodetic rock-uplift rates from this InSAR study (Table S2). All average rates are plotted at the time equivalent to the length of the averaging period. N_{total} is the total number of iterations run and $N_{95\%}$ is the number of iterations within the 95% confidence interval. The yellow bar ranging to 130 ky denotes the range of the Late Quaternary. All model fits can also be plotted as cumulative displacement versus time (Fig. S11).

Accepted Article

© 2017 American Geophysical Union. All rights reserved.

References

Abdrakhmatov, K. Y., et al. (1996), Relatively recent construction of the Tien Shan inferred from GPS measurements of present-day crustal deformation rates, *Nature*, *384*(6608), 450-453, doi:10.1038/384450a0.

Allen, M., J. Jackson, and R. Walker (2004), Late Cenozoic reorganization of the Arabia-Eurasia collision and the comparison of short-term and long-term deformation rates, *Tectonics*, *23*(2), TC2008, doi:10.1029/2003TC001530.

Allmendinger, R. W. (1998), Inverse and forward numerical modeling of trishear fault-propagation folds, *Tectonics*, *17*(4), 640-656, doi:10.1029/98TC01907.

Amos, C. B., D. W. Burbank, and S. A. L. Read (2010), Along-strike growth of the Ostler fault, New Zealand: Consequences for drainage deflection above active thrusts, *Tectonics*, *29*(4), TC4021, doi:10.1029/2009TC002613.

Anders, M. H., and R. W. Schlische (1994), Overlapping Faults, Intrabasin Highs, and the Growth of Normal Faults, *J. Geol.*, *102*(2), 165-179.

Bekaert, D. P. S., A. Hooper, and T. J. Wright (2015a), A spatially variable power law tropospheric correction technique for InSAR data, *J. Geophys. Res.*, *120*(2), 2014JB011558, doi:10.1002/2014JB011558.

Bekaert, D. P. S., R. J. Walters, T. J. Wright, A. J. Hooper, and D. J. Parker (2015b), Statistical comparison of InSAR tropospheric correction techniques, *Remote Sens. Environ.*, *170*, 40-47, doi:http://dx.doi.org/10.1016/j.rse.2015.08.035.

Bettinelli, P., J.-P. Avouac, M. Flouzat, L. Bollinger, G. Ramillien, S. Rajaure, and S. Sapkota (2008), Seasonal variations of seismicity and geodetic strain in the Himalaya induced by surface hydrology, *Earth Planet. Sc. Lett.*, *266*(3–4), 332-344, doi:http://dx.doi.org/10.1016/j.epsl.2007.11.021.

Biasi, G. P., and R. J. Weldon (2006), Estimating Surface Rupture Length and Magnitude of Paleoearthquakes from Point Measurements of Rupture Displacement, *B. Seismol. Soc. Am.*, *96*(5), 1612-1623, doi:10.1785/0120040172.

Bonilla, M. G. (1982), Evaluation of potential surface faulting and other tetonic deformation, *U.S. Geological Survey Open File Report*, *82-0732*, 91.

Bourgois, J., F. Bigot-Cormier, D. Bourles, R. Braucher, O. Dauteuil, C. Witt, and F. Michaud (2007), Tectonic record of strain buildup and abrupt coseismic stress release across the northwestern Peru coastal plain, shelf, and continental slope during the past 200 kyr, *J. Geophys. Res.*, *112*(B4), n/a-n/a, doi:10.1029/2006JB004491.

Bufe, A., D. W. Burbank, L. Liu, B. Bookhagen, J. Qin, J. Chen, J. A. Thompson Jobe, and H. Yang (in revision), Variations of lateral bedrock erosion rates control planation of uplifting folds in the foreland of the Tian Shan, NW China, *J. Geophys. Res.*

Burbank, D., A. Meigs, and N. Brozović (1996), Interactions of growing folds and coeval depositional systems, *Basin Res.*, *8*(3), 199-223, doi:10.1046/j.1365-2117.1996.00181.x.

Cattin, R., and J. P. Avouac (2000), Modeling mountain building and the seismic cycle in the Himalaya of Nepal, *J. Geophys. Res.*, *105*(B6), 13389-13407, doi:10.1029/2000JB900032.

Chen, J., D. W. Burbank, K. M. Scharer, E. Sobel, J. Yin, C. Rubin, and R. Zhao (2002), Magnetochronology of the Upper Cenozoic strata in the Southwestern Chinese Tian Shan: rates of Pleistocene folding and thrusting, *Earth Planet. Sc. Lett.*, *195*(1–2), 113-130, doi:http://dx.doi.org/10.1016/S0012-821X(01)00579-9.

Chen, J., R. Heermance, D. W. Burbank, K. M. Scharer, J. Miao, and C. Wang (2007), Quantification of growth and lateral propagation of the Kashi anticline, southwest Chinese Tian Shan, *J. Geophys. Res.*, *112*(B3), B03S16, doi:10.1029/2006JB004345.

© 2017 American Geophysical Union. All rights reserved.

Accepted Article

Chen, J., T. Li, W.-q. Li, and Z.-d. Yuan (2011), Late Cenozoic and present tectonic deformation in the Pamir salient, northwestern China, *Seismology and Geology*, *33*(2).
Chen, J., K. Scharer, D. Burbank, R. Heermance, and C.-S. Wang (2005), Quaternary detachment folding of the Mingyaole anticline, southwestern Tian Shan, *Dizhen Dizhi (Seismology and Geology)*, *27*(4), 530-547.
Chevalier, M.-L., F. J. Ryerson, P. Tapponnier, R. C. Finkel, J. Van Der Woerd, L. Haibing, and L. Qing (2005), Slip-Rate Measurements on the Karakorum Fault May Imply Secular Variations in Fault Motion, *Science*, *307*(5708), 411-414, doi:10.1126/science.1105466.
Clark, M. K. (2012), Continental collision slowing due to viscous mantle lithosphere rather than topography, *Nature*, *483*(7387), 74-77, doi:10.1038/nature10848.
Davis, K., D. W. Burbank, D. Fisher, S. Wallace, and D. Nobes (2005), Thrust-fault growth and segment linkage in the active Ostler fault zone, New Zealand, *J. Struct. Geol.*, *27*(8), 1528-1546, doi:http://dx.doi.org/10.1016/j.jsg.2005.04.011.
Dawers, N. H., M. H. Anders, and C. H. Scholz (1993), Growth of normal faults: Displacement-length scaling, *Geology*, *21*(12), 1107-1110, doi:10.1130/0091-7613(1993)021<1107:gonfdl>2.3.co;2.
Dee, D. P., et al. (2011), The ERA-Interim reanalysis: configuration and performance of the data assimilation system, *Q. J. Roy. Meteor. Soc.*, *137*(656), 553-597, doi:10.1002/qj.828.
Dolan, J. F., D. D. Bowman, and C. G. Sammis (2007), Long-range and long-term fault interactions in Southern California, *Geology*, *35*(9), 855-858, doi:10.1130/g23789a.1.
Epard, J. L., and R. H. Groshong Jr (1995), Kinematic model of detachment folding including limb rotation, fixed hinges and layer-parallel strain, *Tectonophysics*, *247*(1–4), 85-103, doi:http://dx.doi.org/10.1016/0040-1951(94)00266-C.
Farr, T. G., et al. (2007), The Shuttle Radar Topography Mission, *Rev. Geophys.*, *45*(2), RG2004, doi:10.1029/2005RG000183.
Feng, X. (1994), Surface rupture associated with the 1985 Wuqia earthquake, *Xinjiang: Research on Active Fault*, 45-55.
Friedrich, A. M., B. P. Wernicke, N. A. Niemi, R. A. Bennett, and J. L. Davis (2003), Comparison of geodetic and geologic data from the Wasatch region, Utah, and implications for the spectral character of Earth deformation at periods of 10 to 10 million years, *J. Geophys. Res.*, *108*(B4), 2199, doi:10.1029/2001JB000682.
Gold, R. D., and E. Cowgill (2011), Deriving fault-slip histories to test for secular variation in slip, with examples from the Kunlun and Awatere faults, *Earth Planet. Sc. Lett.*, *301*(1–2), 52-64, doi:http://dx.doi.org/10.1016/j.epsl.2010.10.011.
Gold, R. D., A. Friedrich, S. Kübler, and M. Salamon (2017), Apparent Late Quaternary Fault‐Slip Rate Increase in the Southern Lower Rhine Graben, Central Europe, *B. Seismol. Soc. Am.*, doi:10.1785/0120160197.
Gourmelen, N., T. H. Dixon, F. Amelung, and G. Schmalzle (2011), Acceleration and evolution of faults: An example from the Hunter Mountain–Panamint Valley fault zone, Eastern California, *Earth Planet. Sc. Lett.*, *301*(1–2), 337-344, doi:http://dx.doi.org/10.1016/j.epsl.2010.11.016.
Grant, L. B., and K. Sieh (1994), Paleoseismic evidence of clustered earthquakes on the San Andreas Fault in the Carrizo Plain, California, *J. Geophys. Res.*, *99*(B4), 6819-6841, doi:10.1029/94JB00125.
Gunderson, K. L., et al. (2014), Unraveling tectonic and climatic controls on synorogenic growth strata (Northern Apennines, Italy), *Geol. Soc. Am. Bull.*, *126*(3-4), 532-552, doi:10.1130/b30902.1.

Accepted Article

© 2017 American Geophysical Union. All rights reserved.

Hampel, A., R. Hetzel, and A. L. Densmore (2007), Postglacial slip-rate increase on the Teton normal fault, northern Basin and Range Province, caused by melting of the Yellowstone ice cap and deglaciation of the Teton Range?, *Geology*, *35*(12), 1107-1110, doi:10.1130/g24093a.1.

Heermance, R. V., J. Chen, D. W. Burbank, and J. Miao (2008), Temporal constraints and pulsed Late Cenozoic deformation during the structural disruption of the active Kashi foreland, northwest China, *Tectonics*, *27*(6), TC6012, doi:10.1029/2007TC002226.

Hilley, G. E., and J. R. Arrowsmith (2008), Geomorphic response to uplift along the Dragon's Back pressure ridge, Carrizo Plain, California, *Geology*, *36*(5), 367-370, doi:10.1130/g24517a.1.

Hilley, G. E., K. M. Johnson, M. Wang, Z.-K. Shen, and R. Bürgmann (2009), Earthquake-cycle deformation and fault slip rates in northern Tibet, *Geology*, *37*(1), 31-34, doi:10.1130/g25157a.1.

Hooper, A., D. Bekaert, K. Spaans, and M. Arıkan (2012), Recent advances in SAR interferometry time series analysis for measuring crustal deformation, *Tectonophysics*, *514–517*(0), 1-13, doi:http://dx.doi.org/10.1016/j.tecto.2011.10.013.

Hooper, A., H. Zebker, P. Segall, and B. Kampes (2004), A new method for measuring deformation on volcanoes and other natural terrains using InSAR persistent scatterers, *Geophys. Res. Lett.*, *31*(23), L23611, doi:10.1029/2004GL021737.

Hubert-Ferrari, A., J. Suppe, R. Gonzalez-Mieres, and X. Wang (2007), Mechanisms of active folding of the landscape (southern Tian Shan, China), *J. Geophys. Res.*, *112*(B3), B03S09, doi:10.1029/2006JB004362.

Hussain, E., A. Hooper, T. J. Wright, R. J. Walters, and D. P. S. Bekaert (2016a), Interseismic strain accumulation across the central North Anatolian Fault from iteratively unwrapped InSAR measurements, *J. Geophys. Res.*, 9000–9019, doi:10.1002/2016JB013108.

Hussain, E., T. J. Wright, R. J. Walters, D. Bekaert, A. Hooper, and G. A. Houseman (2016b), Geodetic observations of postseismic creep in the decade after the 1999 Izmit earthquake, Turkey: Implications for a shallow slip deficit, *J. Geophys. Res.*, *121*(4), 2980-3001, doi:10.1002/2015JB012737.

Jackson, J., J.-F. Ritz, L. Siame, G. Raisbeck, F. Yiou, R. Norris, J. Youngson, and E. Bennett (2002), Fault growth and landscape development rates in Otago, New Zealand, using in situ cosmogenic 10Be, *Earth Planet. Sc. Lett.*, *195*(3–4), 185-193, doi:http://dx.doi.org/10.1016/S0012-821X(01)00583-0.

Kampes, B., and S. Usai (1999), Doris: The delft object-oriented radar interferometric software, paper presented at 2nd international symposium on operationalization of remote sensing, enschede, the netherlands, Citeseer.

Kulikova, G. (2015), Source parameters of the major historical earthquakes in the Tien-Shan region from the late 19th to the early 20th century, University of Potsdam, Potsdam.

Li, T., J. Chen, J. A. Thompson, D. W. Burbank, and W. Xiao (2012), Equivalency of geologic and geodetic rates in contractional orogens: New insights from the Pamir Frontal Thrust, *Geophys. Res. Lett.*, *39*(15), L15305, doi:10.1029/2012GL051782.

Li, T., J. Chen, J. A. Thompson, D. W. Burbank, and H. Yang (2015), Hinge-migrated fold-scarp model based on an analysis of bed geometry: A study from the Mingyaole anticline, southern foreland of Chinese Tian Shan, *J. Geophys. Res.*, *120*(9), 6592-6613, doi:10.1002/2015JB012102.

Li, T., J. Chen, J. A. Thompson, D. W. Burbank, and X. Yang (2013), Quantification of three-dimensional folding using fluvial terraces: A case study from the Mushi anticline, northern margin of the Chinese Pamir, *J. Geophys. Res.*, *118*(8), 4628-4647, doi:10.1002/jgrb.50316.

Accepted Article

© 2017 American Geophysical Union. All rights reserved.

Manighetti, I., G. C. P. King, Y. Gaudemer, C. H. Scholz, and C. Doubre (2001), Slip accumulation and lateral propagation of active normal faults in Afar, *J. Geophys. Res.*, *106*(B7), 13667-13696, doi:10.1029/2000JB900471.

Marco, S., M. Stein, A. Agnon, and H. Ron (1996), Long-term earthquake clustering: A 50,000-year paleoseismic record in the Dead Sea Graben, *J. Geophys. Res.*, *101*(B3), 6179-6191, doi:10.1029/95JB01587.

Meade, B. J., and B. H. Hager (2004), Viscoelastic deformation for a clustered earthquake cycle, *Geophys. Res. Lett.*, *31*(10), L10610, doi:10.1029/2004GL019643.

Molnar, P., and J. M. Stock (2009), Slowing of India's convergence with Eurasia since 20 Ma and its implications for Tibetan mantle dynamics, *Tectonics*, *28*(3), TC3001, doi:10.1029/2008TC002271.

Oskin, M., L. Perg, D. Blumentritt, S. Mukhopadhyay, and A. Iriondo (2007), Slip rate of the Calico fault: Implications for geologic versus geodetic rate discrepancy in the Eastern California Shear Zone, *J. Geophys. Res.*, *112*(B3), B03402, doi:10.1029/2006JB004451.

Oskin, M., L. Perg, E. Shelef, M. Strane, E. Gurney, B. Singer, and X. Zhang (2008), Elevated shear zone loading rate during an earthquake cluster in eastern California, *Geology*, *36*(6), 507-510, doi:10.1130/g24814a.1.

Poblet, J., and K. McClay (1996), Geometry and kinematics of single-layer detachment folds, *AAPG Bull.*, *80*(7), 1085-1109.

Qiao, X., P. Yu, Z. Nie, J. Li, X. Wang, S. I. Kuzikov, Q. Wang, and S. Yang (2017), The Crustal Deformation Revealed by GPS and InSAR in the Northwest Corner of the Tarim Basin, Northwestern China, *Pure Appl. Geophys.*, 1-19, doi:10.1007/s00024-017-1473-6.

Rosen, P. A., S. Hensley, G. Peltzer, and M. Simons (2004), Updated repeat orbit interferometry package released, *EOS, Trans. Am. Geophys. Union*, *85*(5), 47-47, doi:10.1029/2004EO050004.

Scharer, K. M., D. W. Burbank, J. Chen, R. J. Weldon, C. Rubin, R. Zhao, and J. Shen (2004), Detachment folding in the Southwestern Tian Shan–Tarim foreland, China: shortening estimates and rates, *J. Struct. Geol.*, *26*(11), 2119-2137, doi:http://dx.doi.org/10.1016/j.jsg.2004.02.016.

Sobel, E. R., J. Chen, and R. V. Heermance (2006), Late Oligocene–Early Miocene initiation of shortening in the Southwestern Chinese Tian Shan: Implications for Neogene shortening rate variations, *Earth Planet. Sc. Lett.*, *247*(1–2), 70-81, doi:http://dx.doi.org/10.1016/j.epsl.2006.03.048.

Sobel, E. R., L. M. Schoenbohm, J. Chen, R. Thiede, D. F. Stockli, M. Sudo, and M. R. Strecker (2011), Late Miocene–Pliocene deceleration of dextral slip between Pamir and Tarim: Implications for Pamir orogenesis, *Earth Planet. Sc. Lett.*, *304*(3–4), 369-378, doi:http://dx.doi.org/10.1016/j.epsl.2011.02.012.

Suppe, J. (1983), Geometry and kinematics of fault-bend folding, *Am. J. Sci.*, *283*(7), 684-721.

Suppe, J., and D. A. Medwedeff (1990), Geometry and kinematics of fault-propagation folding, *Eclogae Geol. Helv.*, *83*(3), 409-454.

Thatcher, W. (1984), The earthquake deformation cycle, recurrence, and the time-predictable model, *J. Geophys. Res.*, *89*(B7), 5674-5680, doi:10.1029/JB089iB07p05674.

Thompson, J. A. (2013), Neogene tectonic evolution of the NE Pamir Margin, NW China, University of California, Santa Barbara, Santa Barbara.

Thompson, J. A., D. W. Burbank, T. Li, J. Chen, and B. Bookhagen (2015), Late Miocene northward propagation of the northeast Pamir thrust system, northwest China, *Tectonics*, 2014TC003690, doi:10.1002/2014TC003690.

Accepted Article

© 2017 American Geophysical Union. All rights reserved.

Thompson, S. C., R. J. Weldon, C. M. Rubin, K. Abdrakhmatov, P. Molnar, and G. W. Berger (2002), Late Quaternary slip rates across the central Tien Shan, Kyrgyzstan, central Asia, *J. Geophys. Res.*, *107*(B9), 2203, doi:10.1029/2001JB000596.

Yan, D.-P., Y.-B. Xu, Z.-B. Dong, L. Qiu, S. Zhang, and M. Wells (2016), Fault-related fold styles and progressions in fold-thrust belts: Insights from sandbox modeling, *J. Geophys. Res.*, 2087–2111, doi:10.1002/2015JB012397.

Zubovich, A. V., et al. (2010), GPS velocity field for the Tien Shan and surrounding regions, *Tectonics*, *29*(6), TC6014, doi:10.1029/2010TC002772.

Accepted Article

© 2017 American Geophysical Union. All rights reserved.